

Low loss mid-infrared ZBLAN waveguides for future astronomical applications

Simon Gross,^{1,2,*} Nemanja Jovanovic,^{1,3,4,5} Adam Sharp,¹ Michael Ireland,^{1,3,4,6} Jon Lawrence,^{1,3,4} and Michael J. Withford^{1,2}

¹ MQ Photonics Research Centre, Dept. of Physics and Astronomy, Macquarie University, NSW 2109, Australia

² Centre for Ultrahigh bandwidth Devices for Optical Systems (CUDOS), Macquarie University, NSW 2109, Australia

³ Macquarie University Research Centre in Astronomy, Astrophysics & Astrophotonics, Dept. of Physics and Astronomy, Macquarie University, NSW 2109, Australia

⁴ Australian Astronomical Observatory (AAO), 105 Dehli Rd, North Ryde, NSW 1710, Australia

⁵ National Astronomical Observatory of Japan (NAOJ), Subaru Telescope, 650 North A'Ohoku Place, Hilo, 96720, HI, USA

⁶ Research School of Astronomy & Astrophysics, Australian National University, Canberra ACT 2611, Australia

*simon.gross@mq.edu.au

Abstract: Photonic technologies will be at the heart of future terrestrial planet hunting interferometers. In particular the mid-infrared spectral region between 3.5 – 4.2 μm is the ideal window for hunting for young extra-solar planets, since the planet is still hot from its formation and thus offers a favorable contrast with respect to the parent star compared to other spectral regions. This paper demonstrates two basic photonic building blocks of such an instrument, namely single-mode waveguides with propagation losses as low as 0.29 ± 0.03 dB/cm at a wavelength of 4 μm as well as directional couplers with a constant splitting ratio across a broad wavelength band of 500 nm. The devices are based on depressed cladding waveguides inscribed into ZBLAN glass using the femtosecond laser direct-write technique. This demonstration is the first stepping stone towards the realization of a high transmission mid-infrared nulling interferometer.

© 2015 Optical Society of America

OCIS codes: (130.0130) Integrated optics; (140.3390) Laser materials processing; (130.2755) Glass waveguides; (130.3060) Infrared.

References and links

1. J. E. Baldwin, C. A. Haniff, C. D. Mackay, and P. J. Warner, "Closure phase in high-resolution optical imaging," *Nature* **320**, 595–597 (1986).
2. A. L. Kraus and M. J. Ireland, "LkCa 15: a young exoplanet caught at formation?," *Astrophys. J.* **745**, 5 (2012).
3. J.-B. Le Bouquin, J.-P. Berger, B. Lazareff, G. Zins, P. Haguenaier, L. Jocou, P. Kern, R. Millan-Gabet, W. Traub, O. Absil, J.-C. Augereau, M. Benisty, N. Blind, X. Bonfils, P. Bourget, A. Delboulbe, P. Feautrier, M. Germain, P. Gitton, D. Gillier, M. Kiekebusch, J. Kluska, J. Knudstrup, P. Labeye, J.-L. Lizon, J.-L. Monin, Y. Magnard, F. Malbet, D. Maurel, F. Ménard, M. Micallef, L. Michaud, G. Montagnier, S. Morel, T. Moulin, K. Perraut, D. Popovic, P. Rabou, S. Rochat, C. Rojas, F. Roussel, A. Roux, E. Stadler, S. Stefl, E. Tatulli, and N. Ventura, "PIONIER: a 4-telescope visitor instrument at VLTI," *Astron. Astrophys.* **535**, A67 (2011).

4. N. Jovanovic, P. G. Tuthill, B. Norris, S. Gross, P. Stewart, N. Charles, S. Lacour, M. Ams, J. S. Lawrence, A. Lehmann, C. Niel, J. G. Robertson, G. D. Marshall, M. Ireland, A. Fuerbach, and M. J. Withford, "Starlight demonstration of the Dragonfly instrument: an integrated photonic pupil-remapping interferometer for high-contrast imaging," *Mon. Not. R. Astron. Soc.* **427**, 806–815 (2012).
5. V. Weber, M. Barillot, P. Haguenaer, P. Y. Kern, I. Schanen-Duport, P. R. Labeye, L. Pujol, and Z. Sodnik, "Nulling interferometer based on an Integrated Optics combiner," *Proc. SPIE* **5491**, 842–850 (2004).
6. R. N. Bracewell, "Detecting nonsolar planets by spinning infrared interferometer," *Nature* **274**, 780–781 (1978).
7. M. Benisty, J.-P. Berger, L. Jocou, P. Labeye, F. Malbet, K. Perraut, and P. Kern, "An integrated optics beam combiner for the second generation VLTI instruments," *Astron. Astrophys.* **498**, 601–613 (2009).
8. S. Martin, A. Booth, K. Liewer, N. Raouf, F. Loya, and H. Tang, "High performance testbed for four-beam infrared interferometric nulling and exoplanet detection," *Appl. Opt.* **51**, 3907–3921 (2012).
9. L. Labadie and O. Wallner, "Mid-infrared guided optics: a perspective for astronomical instruments," *Opt. Express* **17**, 1947–1962 (2009).
10. H.-K. Hsiao, K. A. Winick, J. D. Monnier, and J.-P. Berger, "An infrared integrated optic astronomical beam combiner for stellar interferometry at 3–4 μm ," *Opt. Express* **17**, 18489–18500 (2009).
11. F. Li, S. D. Jackson, C. Grillet, E. Magi, D. Hudson, S. J. Madden, Y. Moghe, C. O'Brien, A. Read, S. G. Duvall, P. Atanackovic, B. J. Eggleton, and D. J. Moss, "Low propagation loss silicon-on-sapphire waveguides for the mid-infrared," *Opt. Express* **19**, 15212–15220 (2011).
12. M. Brun, P. Labeye, G. Grand, J.-M. Hartmann, F. Boulila, M. Carras, and S. Nicoletti, "Low loss SiGe graded index waveguides for mid-IR applications," *Opt. Express* **22**, 508–518 (2014).
13. C. Tsay, Y. Zha, and C. B. Arnold, "Solution-processed chalcogenide glass for integrated single-mode mid-infrared waveguides," *Opt. Express* **18**, 26744–26753 (2010).
14. C. Tsay, E. Mujagić, C. K. Madsen, C. F. Gmachl, and C. B. Arnold, "Mid-infrared characterization of solution-processed As_2S_3 chalcogenide glass waveguides," *Opt. Express* **18**, 15523–15530 (2010).
15. X. Xia, Q. Chen, C. Tsay, C. B. Arnold, and C. K. Madsen, "Low-loss chalcogenide waveguides on lithium niobate for the mid-infrared," *Opt. Lett.* **35**, 3228–3230 (2010).
16. N. Hô, M. C. Phillips, H. Qiao, P. J. Allen, K. Krishnaswami, B. J. Riley, T. L. Myers, and N. C. Anheier Jr., "Single-mode low-loss chalcogenide glass waveguides for the mid-infrared," *Opt. Lett.* **31**, 1860–1862 (2006).
17. A. Ródenas, G. Martin, B. Arezki, N. Psaila, G. Jose, A. Jha, L. Labadie, P. Kern, A. K. Kar, and R. R. Thomson, "Three-dimensional mid-infrared photonic circuits in chalcogenide glass," *Opt. Lett.* **37**, 392–394 (2012).
18. C. D'Amico, G. Cheng, C. Maclair, J. Troles, L. Calvez, V. Nazabal, C. Caillaud, G. Martin, B. Arezki, E. LeCoarer, P. Kern, and R. Stoian, "Large-mode-area infrared guiding in ultrafast laser written waveguides in sulfur-based chalcogenide glasses," *Opt. Express* **22**, 13091–13101 (2014).
19. A. Arriola, S. Mukherjee, D. Choudhury, L. Labadie, and R. R. Thomson, "Ultrafast laser inscription of mid-IR directional couplers for stellar interferometry," *Opt. Lett.* **39**, 4820–4822 (2014).
20. J. M. Parker, "Fluoride Glasses," *Annu. Rev. Mater. Sci.* **19**, 21–41 (1989).
21. D. G. Lancaster, S. Gross, H. Ebendorff-Heidepriem, K. Kuan, T. M. Monro, M. Ams, A. Fuerbach, and M. J. Withford, "Fifty percent internal slope efficiency femtosecond direct-written Tm^{3+} :ZBLAN waveguide laser," *Opt. Lett.* **36**, 1587–1589 (2011).
22. D. G. Lancaster, S. Gross, H. Ebendorff-Heidepriem, A. Fuerbach, M. J. Withford, and T. M. Monro, "2.1 μm waveguide laser fabricated by femtosecond laser direct-writing in Ho^{3+} , Tm^{3+} :ZBLAN glass," *Opt. Lett.* **37**, 996–998 (2012).
23. D. G. Lancaster, S. Gross, A. Fuerbach, H. E. Heidepriem, T. M. Monro, and M. J. Withford, "Versatile large-mode-area femtosecond laser-written Tm :ZBLAN glass chip lasers," *Opt. Express* **20**, 27503–27509 (2012).
24. S. Gross, M. Ams, D. G. Lancaster, T. M. Monro, A. Fuerbach, and M. J. Withford, "Femtosecond direct-write überstructure waveguide Bragg gratings in ZBLAN," *Opt. Lett.* **37**, 3999–4001 (2012).
25. R. R. Thomson, T. A. Birks, S. G. Leon-Saval, A. K. Kar, and J. Bland-Hawthorn, "Ultrafast laser inscription of an integrated photonic lantern," *Opt. Express* **19**, 5698–5705 (2011).
26. A. Arriola, S. Gross, N. Jovanovic, N. Charles, P. G. Tuthill, S. M. Olaizola, A. Fuerbach, and M. J. Withford, "Low bend loss waveguides enable compact, efficient 3D photonic chips," *Opt. Express* **21**, 2978–2986 (2013).
27. S. Gross, M. Ams, G. Palmer, C. T. Miese, R. J. Williams, G. D. Marshall, A. Fuerbach, D. G. Lancaster, H. Ebendorff-Heidepriem, and M. J. Withford, "Ultrafast laser inscription in soft glasses: a comparative study of athermal and thermal processing regimes for guided wave optics," *Int. J. Appl. Glas. Sci.* **3**, 332–348 (2012).
28. G. Tittelbach, B. Richter, and W. Karthe, "Comparison of three transmission methods for integrated optical waveguide propagation loss measurement," *Pure Appl. Opt. J. Eur. Opt. Soc. Part A* **2**, 683–700 (1993).
29. S. Gross, D. G. Lancaster, H. Ebendorff-Heidepriem, T. M. Monro, A. Fuerbach, and M. J. Withford, "Femtosecond laser induced structural changes in fluorozirconate glass," *Opt. Mater. Express* **3**, 574–583 (2013).
30. J. Hu and C. R. Menyuk, "Understanding leaky modes: slab waveguide revisited," *Adv. Opt. Photonics* **1**, 58–106 (2009).
31. A. Snyder and J. Love, *Optical Waveguide Theory* (Springer, 1983), chap. 23.
32. K. Goel and W. Chang, "Extinction ratio degradation due to asymmetry in zero-gap directional coupling and crossing channel switches," *IEEE J. Quantum Electron.* **1**, 2216–2223 (1987).

1. Introduction

The mid-infrared (MIR) spectral region between 3.5 – 4.2 μm , known as the astronomical L' band, is the ideal window to hunt for young extra-solar planets. This is because young planets still warm from the formation process have a peak in their black-body curve in this region while their host stars brightness dims as you move to longer wavelengths, decreasing the relative contrast between the two by orders of magnitude. In addition, although the contrast continues to decrease up to 10 μm , thermal noise swamps the signal making ground-based observations at such long wavelengths challenging. Finally, there is a transmission window in the Earth's atmosphere in the L'-band and the angular resolution of the telescope is higher than compared to 10 μm operation.

The ideal tool to directly image young exoplanets at small angular separation ($\ll 1$ arcsecond) from their host stars is a stellar interferometer. Stellar interferometry relies on combining beams of light from a single target collected by multiple apertures (or 2 parts of the same aperture). By exploiting powerful observables such as the closure phase [1], it is possible to mitigate phase noise due to the atmosphere and the instrument and to calibrate wavefront errors to achieve sub-diffraction limited resolution images. The interferometric technique of aperture masking was recently used in the L-band to image the youngest substellar companion to date [2].

Photonic technologies can and have been applied to stellar interferometry [3, 4]. They offer numerous advantages such as spatial filtering, whereby the corrugated wavefronts of the starlight can be flattened out by propagating the light in the fundamental mode of a single-mode guide which only supports a plane wavefront and thus results in more stable fringes. In particular nulling interferometry can benefit from photonics due to integration and miniaturization, the inherent thermal and mechanical stability as well as reduced degrees of freedom [5]. Nulling interferometry is based on adjusting the phase in one arm of an interferometer such that the star is completely canceled out [6]. As the nearby planet is incoherent with the star's light, it will be seen in the null from the star. In this way the contrast between the bright star and faint companion can be further reduced making the planet visible when using long integration times. Photonic components such as splitters, couplers, X and Y junctions can be used to construct a monolithic beam combining circuit [7], greatly reducing the size and complexity of bulk optic analogs [8]. For the use of photonic elements in astronomical instrumentation their properties must be optimized as follows: losses should be minimized which includes, coupling, Fresnel, propagation, bend and function losses, birefringence should be eliminated, polarization dependent loss minimized and the single-mode region of the guides should be maximized.

Photonic technologies demonstrated at wavelengths longer than 5 μm have been nicely summarized by Labadie *et al.* [9], so we focus our discussion on technologies investigated for the L'-band. Titanium-indiffused waveguides in LiNbO₃ are amongst the best performing devices to date. Propagation losses are < 0.1 dB/cm and on-chip delay lines can be fabricated exploiting the electro-optic effect to scan through the fringe pattern and find the null [10]. However, due to the low numerical apertures (NA) of the guides bend losses are high (0.64 dB/cm and 2 dB/cm for TE and TM polarizations at 22 cm bend radius), the guides exhibit strong unwanted birefringence and the Fresnel reflection losses are substantial due to the high refractive index of LiNbO₃. Lithographically fabricated silicon-on-sapphire nanowires have shown losses of 2 dB/cm at 5 μm [11] despite the fact that the waveguides were not optimized for longer wavelength guidance and had a non-ideal silica overcladding layer which was not transparent at the longer wavelength. In contrast, silicon pedestal waveguides with air cladding showed

losses of 2.7 dB/cm at a wavelength of 3.7 μm . Lower propagation losses were achieved in silicon germanium graded-index waveguides exhibiting 1 dB/cm at 4.5 μm [12]. Besides semiconductors also glass waveguides are promising platforms for the mid-infrared, in particular chalcogenide glass. Tsay *et al.* have demonstrated the fabrication of raised strip waveguides in chalcogenide glass (As_2S_3) by solution-processing and molding techniques, with propagation losses of ≈ 4.5 dB/cm at 4.8 μm [13, 14]. The same group also demonstrated improved propagation losses as low as 0.33 dB/cm for As_2S_3 chalcogenide glass guides by using photolithography and dry-etching techniques [15]. Bend losses for these guides were reported as < 3 dB/cm for bend radii of 250 μm and coupling efficiencies of 81% were theoretically predicted. By using multilayer thin film deposition, channel waveguides in chalcogenide glass have been shown to have propagation losses as low as 0.5 dB/cm and 1.1 dB/cm for the TE and TM polarizations at the slightly longer wavelength of 8.4 μm [16]. Finally, chalcogenide glass has also been successfully used in conjunction with femtosecond laser direct-writing to create MIR single-mode waveguides. Rodenas *et al.* demonstrated a 3-dimensional three beam combiner in gallium lanthanum sulfide glass (GLS) which was single-mode from 3 – 11 μm [17]. However, no propagation losses were reported. In a different chalcogenide glass with the composition of $\text{Ge}_{15}\text{As}_{15}\text{S}_{70}$ propagation losses of ≈ 1 dB/cm at 3.39 μm were achieved in large mode-area multicore waveguides [18]. Arriola *et al.* fabricated straight waveguides and splitters for 3.39 μm with propagation losses as low as 0.8 dB/cm in GLS glass [19]. However, the Fresnel loss at the end-faces alone is large since the refractive index of chalcogenide, just like LiNbO_3 and silicon is relatively high (> 2) adding the complication of multi-layer anti-reflection coatings. Furthermore, fast injection optics are required for planar chalcogenide and silicon waveguides due to their high index contrast.

Until recently fluoro-zirconate glasses such as ZBLAN ($\text{ZrF}_4\text{-BaF}_2\text{-LaF}_3\text{-AlF}_3\text{-NaF}$) have been overlooked due to their tendency to crystallize and their relative fragility and environmental instability when drawn into fibers. However, ZBLAN is an ideal material for the above application as it is highly transparent from 200 nm to above 5 μm [20], and unlike other materials used in the MIR applications, its refractive index is ≈ 1.5 which greatly reduces Fresnel reflection losses. Recently, a suite of devices including waveguide lasers and waveguide Bragg gratings have been demonstrated [21–24] around the 2 μm wavelength region in ZBLAN glass. The devices were fabricated by the femtosecond laser direct-write technique. As only negative index contrast tracks were realized, waveguides were constructed by stitching multiple tracks together to form a depressed cladding. This approach allows for waveguides of arbitrary core size and cladding thickness by simply adding more tracks making it amenable to longer wavelength operation and allowing full control over the span of the single-mode region. Furthermore, since the central region where the majority of the light is confined to is unperturbed by the laser, most of the native properties of the glass such as high transparency and low birefringence remain. Finally, by using the direct-write technique as opposed to lithographic techniques for instance, it is possible to fabricate 3D structures [25, 26]. For these reasons it would be interesting to investigate ZBLAN as a platform for MIR applications, such as the one outlined here as well as for MIR waveguide lasers for chemical sensing applications.

In this body of work we present the performance of ZBLAN waveguides optimized for 4 μm operation fabricated via femtosecond laser direct-writing. In section 2 we outline the fabrication and characterization of the straight waveguides. In section 3 we report the results from the straight guides and discuss losses in detail. Section 4 summarizes the results for the prototype directional coupler followed by some concluding remarks.

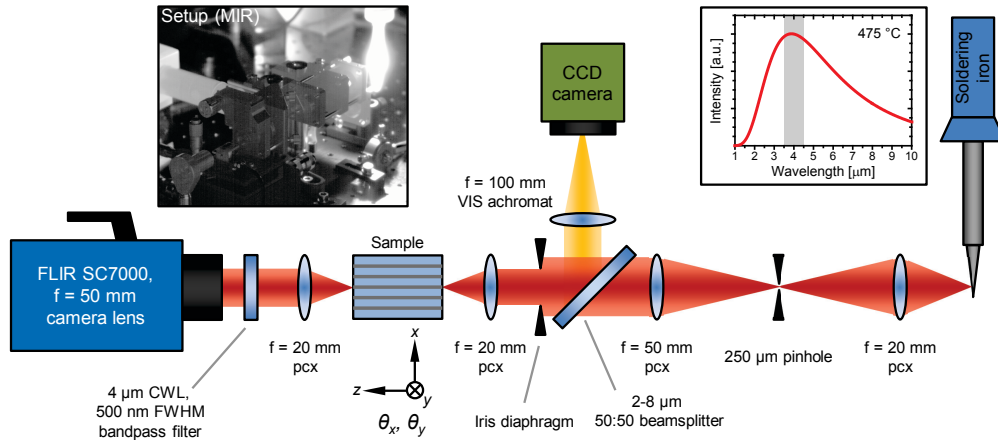


Fig. 1. Sketch of the setup used to characterize the waveguide samples based on thermal radiation emitted by a soldering iron, that is reimaged onto the waveguides using several plano-convex (pcx) CaF_2 lenses. The inset in the top left shows the a photo of the optical setup in the MIR, whereas the inset in the top right is the black-body curve for an object with 475 °C surface temperature. The shaded area corresponds to the transmission band of the used bandpass filter.

2. Fabrication and characterization

The ZBLAN glass was fabricated by the University of Adelaide (using commercially available raw materials) in a controlled atmosphere glass melting facility to cast 50 g glass ingots. To create the waveguide substrates the ingot was diced into 3 chips measuring 39 mm length, 12 mm width and 3 mm height by a CNC diamond saw. The top and bottom faces of each sample were polished to allow the femtosecond laser to be focused below the surface, with the waveguide axes set at a depth of 300 μm . The waveguides were inscribed using pulses from an ultrafast Ti:sapphire oscillator (FEMTOSOURCE XL 500 - Femtolasers GmbH, 800 nm center wavelength, <50 fs pulse duration, 5.1 MHz repetition rate), which were focused into the chip using a 1.25 NA 100 \times oil immersion objective (Zeiss N-Achroplan) while the sample was translated using a set of computer controlled XYZ air-bearing translation stages. As the index change induced by the writing laser was negative in nature [27], then depressed cladding guides were created by stitching partially overlapping rings of depressed index laser tracks together. The chip described here contained 12 waveguides separated by 900 μm with core diameters ranging of 35, 40 and 45 μm , and cladding width of 30, 40, 50 and 60 μm . The smallest waveguide (35 μm core, 30 μm cladding) was composed of 34 individual laser modifications arranged in 2 concentric rings, whereas the largest waveguide (45 μm core, 60 μm cladding) had 100 modifications of 20 μm diameter each arranged on 4 concentric rings. To ensure sufficient overlap between the individual 20 μm modifications for creating a continuous cladding, the radii of the concentric rings was increased using a maximum step size of 15 μm . The waveguides were written bottom up with a pulse energy of 65 nJ and a translation speed of 1000 mm/min. After waveguide writing, two of the chips were cut up into shorter samples which resulted in 4 samples which were 10.5, 24.9, 31.0 and 36.3 mm long post grinding and polishing of the end-faces.

A soldering iron with a surface temperature of 475 °C and a peak in the black-body curve at $\approx 4 \mu\text{m}$ (see inset in Fig. 1) was used as the light source for probing the guides. Unlike high coherence sources such as HeNe and quantum cascade lasers, the low-coherence of the thermal

source avoids Fabry-Pérot effects within the glass waveguide caused by Fresnel reflections off the end-faces [28] and it thus enables highly accurate cut-back loss measurements. The surface of the soldering iron tip was reimaged onto a $250\ \mu\text{m}$ pinhole with the aid of a 20 mm focal length uncoated plano-convex CaF_2 lens. The light from the pinhole was collimated with a 50 mm focal length uncoated plano-convex CaF_2 lens before passing through a beamsplitter, an iris and a 20 mm focal length uncoated plano-convex CaF_2 to focus the light onto the input facet of the sample. The iris was used to control the beam size before the last lens and thereby the focal ratio (F-number, $F/\#$) of the injected quasi flat-top beam. The chip was mounted on a 3+2-axis (XYZ and θ_x, θ_y) stage in order to precisely align it. The soldering iron was temporarily replaced by a $400\ \mu\text{m}$ multimode fiber which delivered light from a green LED. A CCD camera was used to coarsely align the green spot with each waveguide core laterally by temporarily changing the sample's z-axis position to put it in focus at the green wavelength. Once aligned, the sample's z-axis position was returned to the infrared focus, and the green fiber was replaced with the soldering iron. The output light was recollimated by a 20 mm focal length uncoated plano-convex CaF_2 lens before being focused onto a InSb camera (Flir SC7000, 640×512 pixels) with a 50 mm camera lens. A bandpass filter centered at $4\ \mu\text{m}$ (500 nm FWHM) was used to select the spectral content and it was placed right in front of the camera to minimize stray thermal light. The encircled flux of the reimaged point-spread function (PSF) was maximized by carefully maneuvering the guide with the translation stage. An image of the waveguide near-field was captured in this way. The throughput for each guide was compared to the injected beam without the chip in the way, post dark subtraction. Note the imaging assembly was translated toward the beam by the length of the chip to image the injected beam. A similar method was utilized for the coupler as well. The propagation losses were determined by plotting the raw throughputs for each waveguide versus the chip length on a semi-log scale, followed by a least-square fit where the obtained slopes correspond to the propagation losses.

3. Waveguide numerical aperture and propagation losses

The numerical aperture (NA) of the waveguides was determined by measuring the waveguide transmission at different focal ratios ($F/\#$) of the injected beam. The $F/\#$ was adjusted by opening or closing the iris in front of the injection lens. A plot of the transmission against $F/\#$ for 3 waveguides with different dimensions is illustrated in Fig. 2(a). The scatter of the data points is a result of the data processing for determining the integrated intensities from the measured near-field profiles. This process is background sensitive, in particular to a non-uniform background resulting from scattered light, which is caused by the poor mode-matching between the waveguide and quasi flat-top injection spot since the injection spot is multi-mode with a high number of modes for low $F/\#$ s.

For small $F/\#$ (high injection numerical aperture) the waveguides exhibit a low transmission because light is injected beyond the waveguides acceptance angle. With increasing $F/\#$ the transmission increases until it reaches a plateau where the NA of the injected beam is smaller than the acceptance NA of the waveguides. The plateau in transmission can be related to the fact that the injected spot size was constant throughout the experiment (as it was the image of a pinhole) and thus this experiment reveals the nature of coupling to the guide only as a function of NA. In contrast, when injecting a spot that changes its size with NA (by changing focusing lenses for example), the transmission would exhibit a clear maximum where the injected beam best matches the waveguide mode, and decreased transmission for NA higher and lower than the optimum.

All three tested waveguides with different geometrical parameters show identical cut-offs of $F/\# = 12 \pm 1$, which is expected since the NA only depends on the index contrast and

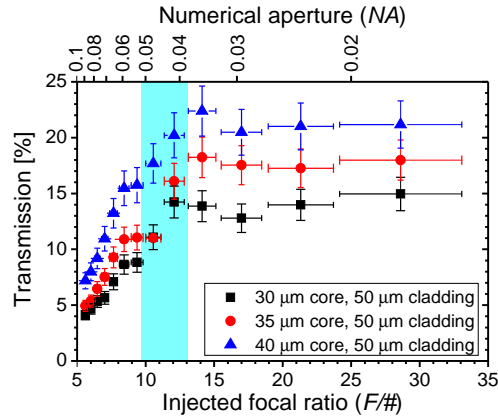


Fig. 2. Waveguide transmission as a function of the injected focal ratio and the corresponding numerical aperture for 3 different waveguides. All waveguides show identical focal ratios of $F/\# = 12 \pm 1$ or the equivalent numerical apertures of $NA = 0.042 \pm 0.004$. The blue bar indicates the numerical aperture $NA = 0.046 \pm 0.007$ of the waveguides as determined by comparing the experimentally measured to the computed mode-field diameters using a step-index profile.

not the geometrical waveguide parameters. This $F/\#$ corresponds to a numerical aperture of $NA = 0.042 \pm 0.004$ ($NA \approx 1/(2 F/\#)$). For sufficiently wide claddings, the waveguides can be approximated by a standard step-index waveguide. Therefore the numerical aperture and the index contrast of the waveguide are related by $NA = \sqrt{n_{co}^2 - n_{cl}^2}$, where n_{co} and n_{cl} are the core and cladding refractive indices, respectively. This results in an index contrast of $\Delta n = -(6 \pm 1) \times 10^{-4}$. When computing the guided mode using RSoft BeamPROP for various index contrasts and comparing the computed to the measured near-field profile, an index contrast of $\Delta n = -(7 \pm 2) \times 10^{-4}$ ($NA = 0.046 \pm 0.007$) was found in close agreement with the focal ratio approach. For comparison, in multicomponent silicate glass as well as in chalcogenide glass laser induced index changes in the order of $+10^{-2}$ have been reported [17, 26]. Furthermore in ZBLAN at 635 nm wavelength, index contrasts in the order of -1 to -1.5×10^{-3} were measured using a refracted near-field profiler [21, 29]. This indicates that there is a differential chromatic dispersion between the modified and bulk material which leads to a difference in index contrast as a function of wavelength.

The measured propagation losses, as shown in Fig. 3(a), follow the general trend predicted by simulations as illustrated in Fig. 3(b). Larger cores and wider claddings result in reduced propagation losses due to less leakage through the finite cladding. This loss is characteristic for depressed cladding waveguides since they only support a continuum of radiation modes that closely resemble the shape of a truly guided mode [30]. This results in an exponential decay of the light as it propagates in the waveguide. The confinement losses increase for decreasing depressed cladding width as well as decreasing index contrast. These intrinsic confinement losses at a wavelength of $4 \mu\text{m}$ were computed using RSoft BeamPROP for an ideal step-index depressed ring with varying core and cladding size for an index contrast of $\Delta n = -9 \times 10^{-4}$. The index contrast is an upper limit for the experimentally determined index contrast of the inscribed waveguides via their mode-field diameters and therefore the computed confinement losses can be seen as a lower bound. The confinement losses of an ideal depressed cladding waveguide are shown in Fig. 3(b) (note the different scale). The lowest measured loss was 0.29 ± 0.03 dB/cm for a waveguide with a measured core diameter of $47 \mu\text{m}$ and a $59 \mu\text{m}$ wide

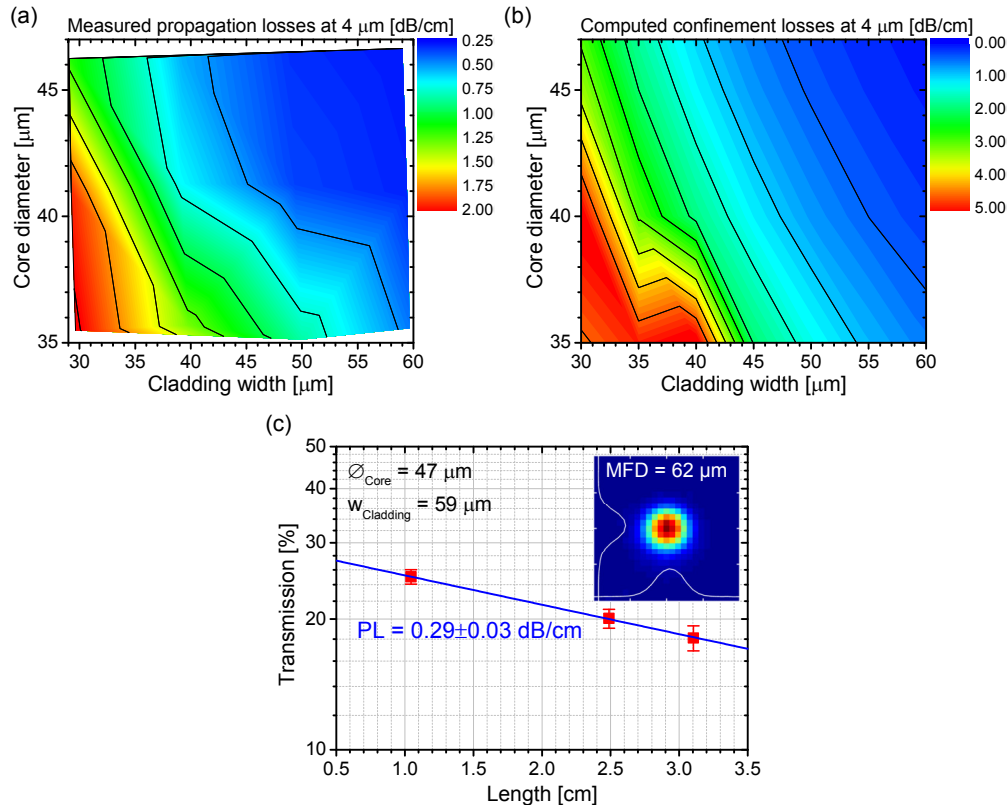


Fig. 3. (a) Measured propagation losses as function of the waveguide core diameter and width of the surrounding cladding. (b) Computed intrinsic confinement losses of the depressed cladding geometry due to leakage through the finite cladding. The losses are plotted as a function of core diameter and cladding width for an index contrast of $\Delta n = -9 \times 10^{-4}$, which is the upper limit for the experimentally determined index contrast. (c) Transmission of the lowest loss waveguide ($47 \mu\text{m}$ core diameter and $59 \mu\text{m}$ cladding width) as a function of the sample length. The linear fit corresponds to a propagation loss (PL) of $0.29 \pm 0.03 \text{ dB/cm}$. The inset shows the corresponding near-field profile of the waveguide.

cladding as illustrated in Fig. 3(c). Based on the simulations, such a waveguide has confinement losses of 0.18 dB/cm indicating the presence of scattering and bulk absorption losses. However, the confinement losses still make up a considerable portion of the propagation losses. Therefore, a further improvement in propagation losses should be achievable by increasing the cladding width and/or the core diameter. For narrow claddings and small cores where the waveguides are only weakly guiding, the computed confinement losses exceed the measured propagation losses. This is likely a result of stress within the waveguides, which slightly raises the refractive index of the waveguide core with respect to the bulk glass which was not accounted for in the simulations. In fact, stress fractures can appear during inscription at the outer edges of the depressed claddings [21], however, without any detrimental effect on the waveguide performance. In fact, the induced stress by the laser inscribed modifications is intrinsic to the refractive index change, which is based on a physical expansion of the glass network [29]. The occurrence of stress fractures can be mitigated by placing the waveguides deeper within the glass. In the present work the depth was limited by the working distance of the microscope objective.

The inset in Fig. 3(c) shows the corresponding near-field profile for the lowest loss waveguide. The $1/e^2$ mode-field diameter obtained by fitting a Gaussian function is $62 \mu\text{m}$. A circular mode is important for the efficient injection of light from an astronomical telescope since simple circular microlenses can be used in contrast to high index contrast ridge waveguides that usually exhibit non-circular mode-profiles. It should be noted, that the raw throughput of only $\approx 30\%$ in Fig. 3(c) is a result of the coupling losses because the waveguides were illuminated with a quasi top-hat intensity distribution of $\approx 100 \mu\text{m}$ diameter as well as 7% Fresnel reflection losses.

4. Depressed cladding directional coupler

Key elements of an astronomical nulling interferometer are directional couplers. Therefore the feasibility of creating a low loss directional coupler based on the presented depressed cladding geometry was investigated. The device was inscribed using waveguides with $60 \mu\text{m}$ cladding and a slightly larger core of $50 \mu\text{m}$ diameter to further reduce the confinement and hence propagation losses. Despite the larger core, the waveguides were still single-mode at the short wavelength edge of the bandpass filter ($3.75 \mu\text{m}$) with a V number of $V \approx 1.8$. The waveguides, spaced by $150 \mu\text{m}$ at the input and output of the device, were brought into close proximity using raised-sine bends with a length of 16 mm to reach a core-to-core spacing of $40 \mu\text{m}$ in the interaction region of the coupler. The total device length was 33.6 mm. These parameters resulted in minimum bend radii of 313 mm in order to reduce bend losses arising from the low index contrast of the waveguides. When approximating the waveguides by a step-index with an index contrast of $\Delta n = 7 \times 10^{-4}$ the predicted transmission per raised-sine bend is $\approx 80\%$ using the analytical solution for a step-index waveguide [31]. As a result of the gradual raised-sine bends, simulations based on the experimentally determined index contrast predicted close to 3 dB splitting for 0 mm interaction length, i.e. without a straight waveguide section between the two raised-sine bend. The small core spacing of $40 \mu\text{m}$ meant that the two $50 \mu\text{m}$ cores were merged in the interaction region avoiding laser modified glass in between. Such a zero-gap directional coupler is based on two-mode interference in the interaction region [32]. In principal, nearly arbitrary spacing can be achieved without perturbing the waveguide cladding geometry, except for spacings where there is still a gap between the two cores that is less

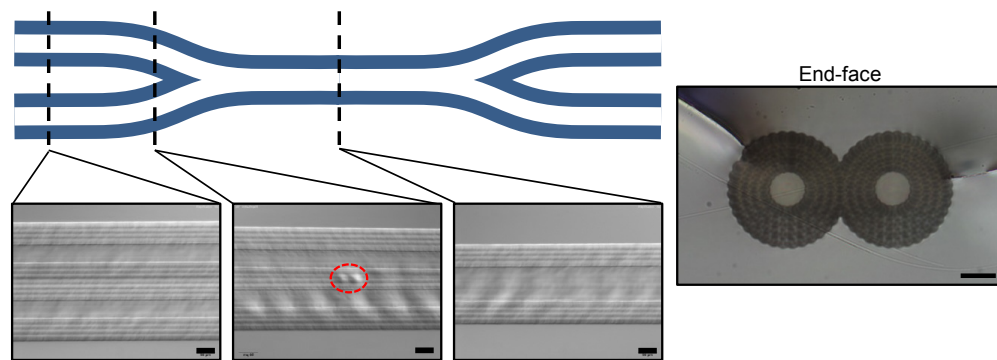


Fig. 4. Sketch of the depressed cladding directional coupler with transmission differential interference contrast microscope images taken at different positions of the device. The scale bar in the images corresponds to $50 \mu\text{m}$. The red dashed circles marks defects created by hard on/off switching of the laser. On the right-hand side an image of the coupler's end-face is shown. Stress-fractures are apparent at the edges of the cladding, however without affecting the waveguide performance. The inscription laser was incident from the top.

than the diameter of an individual modification ($20\ \mu\text{m}$ in this case). In other words, in that case smaller modifications would be required in order to exactly fill the gap between the two cores. The entire directional coupler was inscribed bottom up like the straight waveguides, i.e. alternating between modifications of the left and right waveguide, respectively. To create the coupling region, the laser was switched off once a modification would cross the middle plane of the device. Figure 4 shows a sketch of the coupler including microscope images taken at different sections of the device showing the transition from two individual waveguide cores to a single wide core in the interaction region. Due to hard switching the laser on and off small defects occur at the ends of individual modifications as highlighted by the red dashed circle in Fig. 4. These defects can be a source of additional loss but should be avoidable by smoothly turning the laser power down and up, i.e. tapering, rather than hard switching.

The splitting ratio of the device was measured using the setup in Fig. 1. However, the $250\ \mu\text{m}$ pinhole was replaced for a $200\ \mu\text{m}$ pinhole resulting in a $80\ \mu\text{m}$ as opposed to a $100\ \mu\text{m}$ spot on the chip end-face to ensure that light is exclusively injected into a single waveguide. Furthermore, a CaF_2 prism with an apex angle of 69.9° was added between the collimating lens and camera lens in order to spectrally disperse the output resulting in a resolving power $R = \lambda/\Delta\lambda \approx 35$. Figure 5 shows the splitting ratio as a function of wavelength. Identical splitting ratios and transmission values within the accuracy of measurement were observed when either injecting into the first or second waveguide. The depressed cladding coupler shows a splitting ratio of 75:25 at the centre wavelength with a variation of only $\pm 6\%$ across the $500\ \text{nm}$ wavelength band. This broad operation band makes it ideal for astronomical interferometry. A further improvement of the operational bandwidth can be achieved by optimizing the wavelength dependent bend induced phase and/or by introducing asymmetry by the means of cores of different size and/or index contrast [33]. Unlike in conventional laser written positive index contrast waveguides, the depressed cladding approach permits straight forward independent control over the index contrast and waveguide core size. The insertion loss of the coupler when injecting a $F/\# = 14$ beam is $4.4\ \text{dB}$. For comparison, a straight waveguide of equal length with a $45\ \mu\text{m}$ core and $50\ \mu\text{m}$ cladding (propagation loss of $0.34 \pm 0.06\ \text{dB/cm}$) has insertion losses of $5.2\ \text{dB}$ under identical injection conditions and a $40\ \mu\text{m}$ core and $60\ \mu\text{m}$ cladding waveguide (propagation loss of $0.31 \pm 0.02\ \text{dB/cm}$) exhibits insertion losses of $4.8\ \text{dB}$. It should be noted that the coupling efficiency into the directional coupler is higher due to the larger core. Nevertheless, it shows that no significant losses are introduced neither by the bends nor the laser

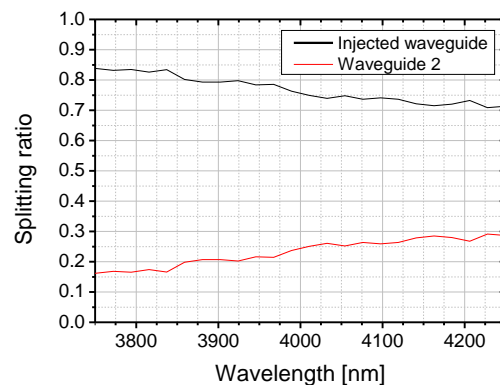


Fig. 5. Splitting ratio of the depressed cladding directional coupler prototype across a wavelength band from 3.75 to $4.25\ \mu\text{m}$.

induced defects.

In order to further improve the transmission the index contrast has to be increased, thereby enabling the use of shorter raised-sine bends. This can be achieved by either overpassing the individual modifications multiple times or by inscribing the cladding using kHz instead of MHz repetition rate laser pulses [27]. Low repetition rate, athermal fabrication results in an up to 3-fold increase of the refractive index contrast at the expense of a greatly increased fabrication time.

5. Conclusion

The femtosecond laser inscription of mid-infrared single-mode waveguides into ZBLAN glass was successfully demonstrated. The waveguides are based on a depressed cladding due to the laser induced reduction of the refractive index with respect to the bulk glass. ZBLAN's high transparency in the mid-infrared in combination with the depressed cladding architecture has enabled propagation losses as low as 0.29 ± 0.03 dB/cm at a wavelength of $4 \mu\text{m}$. Furthermore, the geometric flexibility of the depressed cladding architecture enabled circular mode-profiles, ideal for the low loss injection of stellar light from an astronomical telescope. In addition, a depressed cladding directional coupler with a low splitting ratio variation across a wavelength band of 500 nm centred at $4 \mu\text{m}$ was demonstrated. Despite the waveguide's low index contrast of $< 1 \times 10^{-3}$, the splitter features insertion losses comparable to a straight waveguide. These waveguides and directional couplers hold great potential for future integrated pupil remappers and nulling interferometers for the detection of exoplanets.

Acknowledgments

This research was supported by the Australian Research Council Centre of Excellence for Ultrahigh bandwidth Devices for Optical Systems (project number CE110001018) and was performed in part at the OptoFab node of the Australian National Fabrication Facility utilizing Commonwealth as well as NSW and SA State Government funding. S. Gross acknowledges a Macquarie University Research Fellowship (MQRF).